Delft University of Technology

Flight-Path Reconstruction and Flight Test of Four-Line Power Kites

Borobia-Moreno, R.; Sánchez-Arriaga, Gonzalo; Serino, A.; Schmehl, Roland

Flight-Path Reconstruction and Flight Test of Four-Line Power Kites

R. Borobia* and G. Sanchez-Arriaga†
Charles III University of Madrid, 28911 Leganés, Spain
A. Serino‡
Polytechnic University of Turin, 10129 Torino, Italy
and
R. Schmehl§
Delft University of Technology, 2629 HS Delft, The Netherlands

A flight-path reconstruction algorithm for tethered aircraft, which is based on an extended Kalman filter, is presented. The algorithm is fed by the measurements of a set of onboard and ground-based instruments and provides the optimal estimation of the system state-space trajectory, which includes typical aircraft variables such as position and velocity, as well as an estimation of the aerodynamic force and torque. Therefore, it can be applied to closed-loop control in airborne wind energy systems and it is a first step toward aerodynamic parameter identification of tethered aircraft using flight-test data. The performance of the algorithm is investigated by feeding it with real flight data obtained from a low-cost and highly portable experimental setup with a four-line kite. Several flight tests, which include pullup and lateral-directional steering maneuvers with two kites of different areas, are conducted. The coherence of the estimations provided by the filter, such as the kite state-space trajectory and aerodynamic forces and torques, is analyzed. For some standard variables, such as kite Euler angles and position, the results are also compared with a second independent onboard estimator.

Nomenclature

B	=	magnetic field, T
D_{cb}	=	control bar displacement, m
$\tilde{d}_{\pm}$	=	distance sensor measurements, m
F_a	=	aerodynamic force, N
$\tilde{f}_{IMU}$	=	specific force, m/s^2
L_{cb}	=	length of the control bar, m
L_{ds}	=	depower stopper distance, m
L_l	=	lengths of the frontal lines, m
L_{ps}	=	power stopper distance, m
L_s	=	length of the sliding tether, m
L_t	=	lengths of the rear lines, m
M_a	=	aerodynamic torque, N/m
m	=	kite mass, kg
p_d	=	differential pressure, Pa
$\bar{Q}$	=	process covariance matrix
$\bar{R}$	=	observation covariance matrix
$\bar{R}_{EK}$	=	Earth to kite body axis rotation matrix
r	=	kite position, m
S	=	kite surface, m^2
s_0	=	control bar to load cell distance, m
T	=	tether tension, N
u_p	=	power ratio of the control bar
v	=	kite velocity, m/s
w_{cl}	=	width of the chicken-loop interface, m
$\hat{x}$	=	estimated value of x
$\tilde{x}$	=	measured value of x

y	=	measurement vector given by sensors
η	=	sensor noise
Θ	=	instrument bias
θ	=	pitch angle, rad
ν	=	control bar deflection angle, rad
ρ	=	air density, kg/m^3
σ^2	=	variances
Υ	=	Euler angles vector, rad
ϕ	=	roll angle, rad
χ	=	Markov state vector
ψ	=	yaw angle, rad
ω	=	kite angular velocity, rad/s

Subscripts and accents

$A_{\pm}$	=	leading edge attachment points
$B_{\pm}$	=	trailing edge attachment points
E	=	Earth frame
K	=	kite body frame
k	=	kite
$\hat{x}$	=	estimated value of a variable
$\tilde{x}$	=	observed value of a variable

I. Introduction

THE increasing demand for renewable energy is actively driving the search for more efficient methods to harvest energy from the wind. Although conventional horizontal-axis wind turbines now play an important role in the energy economy of many countries, the technology has a substantial environmental impact and, particularly for offshore deployment, is still relatively expensive. This triggered the research on airborne wind energy (AWE) systems based on the pioneering work of Miles Loyd [1]. These devices operate at higher altitudes than conventional wind turbines where, due to more steady and stronger winds, more energy is available. The proposed solutions include the so-called ground- and fly-generation systems (see a review of technologies in Refs. [2,3]). For a ground-generation system, the high tether tension obtained by flying the kite along optimal crosswind trajectories is used to drive a drum with a connected generator on the ground in a pumping cycle with alternating reel out and reel in [4,5]. Fly-generation systems produce the electrical power

directly on board by using wind turbines [6]. An example is Makani's M600 system, developed by Makani Power in the United States [7].

To become a real alternative to other energy generation systems, AWE systems need to operate autonomously for long periods of time and be efficient in a broad range of wind speeds. However, the design of wind energy systems based on power kites and capable of operating autonomously for extended periods of time is technically challenging. Similar to any other unmanned air vehicle, several disciplines (such as system state estimation, control, and guidance) are interrelated. The aerodynamic characterization of the kite also plays a central role both in the design and evaluation of the system capabilities. The flexible nature of the kite structure, the constraints imposed by the tethers, and the lack of accurate aerodynamic data are rendering the development of these systems difficult. For these reasons, the development of accurate mathematical models validated by flight testing is a priority for the AWE community. In this regard, testbeds for airborne wind energy technologies [8], as well as flight simulators [5,9–15], are of great interest. Naturally, these last include an aerodynamic model, which basically receives the airspeed of the kite and returns the aerodynamic coefficients that describe the aerodynamic force and torque about the center of mass of the kite. These coefficients, which are also denoted as stability derivatives, play a central role in the stability of the equilibrium of the kite [16,17], which is of fundamental interest for many kite applications including the generation of energy. Although analyses with computational fluid dynamics codes have been carried out [18,19], the complex fluid–structure interaction is still an open and active field of research. Wind-tunnel experiments for ram-air wings have been also conducted [20].

On the other hand, in addition to numerical and wind-tunnel studies, aircraft aerodynamic characterization based on real flight-test data has been used profusely by the aerospace industry in the past. This characterization can be approached by both in one-step or two-step techniques. One-step techniques, such as the maximum likelihood method, estimate both the state variables and the aerodynamic parameters at the same time by an optimization process. This is done by a formulation of the process model that implicitly includes the aerodynamic coefficients, requiring an a priori knowledge of the structure of the aerodynamic model [21,22]. A study on kite aerodynamic identification with estimations of the generated lift and drag, and based on some a priori system modelization, has been presented recently [23]. Two-step techniques [or estimation before modeling (EBM) [24,25]] first estimate the time histories of the state variables of the system. Such time histories, which include the aerodynamic force and moment, are used in the second phase to perform the aerodynamic parameters identification of the system. Because of the space state trajectory estimation, the so-called flight-path reconstruction (FPR) [26] is independent of the proposed aerodynamic model structure, a priori knowledge of the system is no longer needed, and different model structures can be tested afterward without a reformulation of the problem. For this reason, the solution of the FPR problem is the first step toward aerodynamic parameter identification for AWE systems. Recent works have tackled this problem for rigid-wing AWE pumping systems [27,28].

Our contribution consists of two main elements. The first one is a portable and low-cost experimental setup for the acquisition of flight data from four-line kites with tether lengths on the order of several tens of meters. Recent works highlighted the important role of these types of experiments in the progress of AWE systems and the difficulties arising in the determination of the airspeed of the kite [29,30]. The second element is a solution for the kite FPR problem, which incorporates special features of this type of system such as the constraints imposed by the tethers and their tensions. For configurations with relatively short lines, tether sagging can be neglected and the accuracy of the Global Positioning System (GPS) can be improved by the geometric constraint introduced by the lines [31,32].

The work is organized as follows. Section II describes the main elements of the experimental setup and justifies the hardware selection. Two different four-line power kites are used as platforms, and a set of measurement instruments provides state variables, such as position, velocity, acceleration, attitude, angular acceleration, airspeed, and tether tension. Control variables (i.e., the position of the control bar) are

also measured during the flight tests. Two key features of the setup are the low cost and portability because it can be easily adapted to other types of kites. An outline of the FPR algorithm is given in Sec. III, and its full description is in the Appendix. The experimental results and the performance of the FPR method are given in Sec. IV, whereas the conclusions and applications of the work are presented in Sec. V.

II. Experimental Setup

A. System Layout

Figure 1 shows a schematic of the experimental setup. It involves a four-line power kite of mass m and surface S attached to a fixed point O_E on the ground. In our experimental setup, point O_E coincides with the hook of a stationary car that acts as a large mass to anchor the system. Point O_E is the origin of an Earth-fixed reference frame S_E with axes x_E and y_E spanning the horizontal ground and pointing to the north and east, respectively, with z_E pointing downward. In the following, the frames of reference are denoted with capital letters. The two front tethers, attached to the leading edge of the kite at points $A_\pm$, are of lengths L_l and connect at point F_v. The two control tethers of lengths L_t connect points $B_\pm$ of the trailing edge with the tips of a control bar of length L_{cb}. The control bar slides over a short tether of length L_s that links the moving point F_v with the origin O_E fixed to the ground. Following Ref. [17], we also introduce the plane Π defined by points F_v and $A_\pm$ (see Fig. 2). Because the tethers
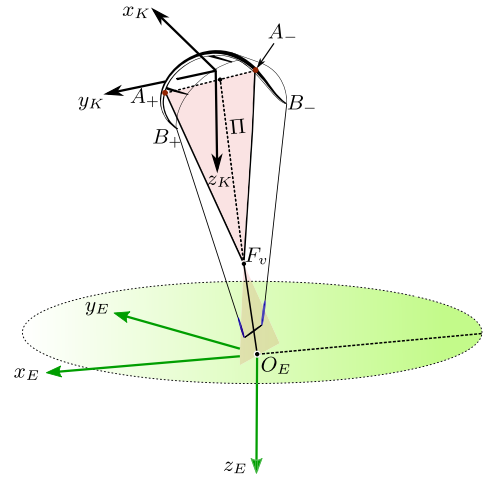
Fig. 1   Frames of references and scheme of the experimental setup.
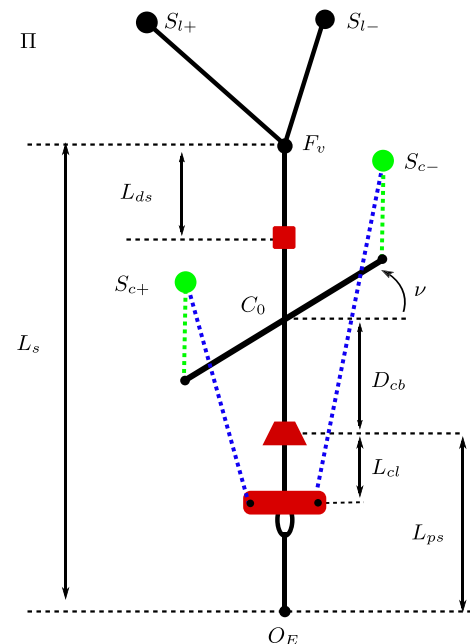
Fig. 2   Detail of the Π plane.

connected to the leading-edge transfer most of the aerodynamic load, we will assume that they are well tensioned, and thus straight within the plane Π. A kite-fixed reference frame S_K linked to the kite with an origin at its center of mass O_K will also be used. Axes x_K and z_K are in the plane of symmetry of the kite, x_K is parallel to the center chord (i.e., the imaginary line linking the leading- and trailing-edge points of the plane of symmetry of the kite), and y_K completes a right-handed coordinate frame. Because the kite has a plane of symmetry, the S_K component of the tensor of inertia of the kite about its center of mass then reads

$$\bar{I}_{O_K} = \begin{pmatrix} I_x & 0 & I_{xz} \\ 0 & I_y & 0 \\ I_{xz} & 0 & I_z \end{pmatrix} \qquad (1)$$

and $I_{xy} = 0$ and $I_{yz} = 0$.

Our kite state vector

$$\boldsymbol{x}_k = [\boldsymbol{r} \quad \boldsymbol{v} \quad \boldsymbol{\Upsilon} \quad \boldsymbol{\omega}] \qquad (2)$$

includes the S_E components of the position vector of the kite; the S_K components of the absolute velocity and angular velocity of the kite; and its roll, pitch, and yaw angles:

$$\boldsymbol{r} = \overline{O_E O_K} = x_E \boldsymbol{i}_E + y_E \boldsymbol{j}_E + z_E \boldsymbol{k}_E \qquad (3)$$

$$\boldsymbol{v} = d\boldsymbol{r}/dt = u \boldsymbol{i}_K + v \boldsymbol{j}_K + w \boldsymbol{k}_K \qquad (4)$$

$$\boldsymbol{\omega} = p \boldsymbol{i}_K + q \boldsymbol{j}_K + r \boldsymbol{k}_K \qquad (5)$$

$$\boldsymbol{\Upsilon} = [\phi \quad \theta \quad \psi] \qquad (6)$$

A detail of the configuration of the control bar is given in Fig. 2. The middle point of the bar, named C_0, slides over a tether of length L_s that links points F_v and O_E. If considered massless, such a tether will be in the Π plane because its tension vector is in equilibrium with the tension vectors of the two tethers connecting to the leading edge that define the Π plane. The movement of the bar is limited by the depower and power stoppers that are placed at distances L_{ds} and L_{ps} from F_v and O_E, respectively. Its distance to the power stopper is denoted as D_{cb}. Assuming that the pilot maneuvers the kite while keeping the control bar inside plane Π, the state of the bar is given by a control vector with only two variables:

$$\boldsymbol{x}_c = [u_p \quad \nu] \qquad (7)$$

i.e., a power ratio u_p and the bar deflection angle ν between the bar and the tether of length L_s. The former is defined as [29]

$$u_p = 1 - \frac{D_{cb}}{L_s - L_{ps} - L_{ds}} \qquad (8)$$

and it takes values equal to zero and one when the kite is fully depowered (bar at the depower stopper) and powered (bar at the power stopper), respectively. Figure 2 also shows the four load sensors (marked by symbols $S_{c\pm}$ and $S_{l\pm}$) and the distance sensors attached to the control bar safety fuse just below the depower stopper. These elements are described in Sec. II.B, which focuses on the hardware selection and the reconstruction of the state and control vectors from the measurements.

B. Hardware Selection

AWE systems are being developed on the basis of flexible ram-air kites (KiteEnergy, Kite Power Systems, and SkySails), semirigid inflatable kites (Kitepower), and tethered fixed-wing drones (Makani/X or Ampyx Power) [2] flying hundreds of meters high in the sky. Because the rigid-body hypothesis is implicitly assumed in our work, our solution to the FPR problem is more suitable for semirigid and tethered fixed-wing drones. This assumption, in addition to cost and resource constraints, leads to the decision to focus the analysis on two different four-line off-the-shelf inflatable surf kites with tether lengths on the order of several tens of meters. These kites, although smaller scale, are still representative of the ones used in AWE systems and show the portability of our experimental setup. Moreover, the techniques, tools, and hardware components developed in this work can be easily implemented with much larger kites. The two selected kites, having different areas and numbers of struts (stiffness), also provide a broad wind speed range without switching to different-scaled load sensors. Table 1 shows the most important characteristics of the kites. They both have the same mass, but there is a 30% difference in surface area. Compared to the larger kite, the smaller one is more rigid because it has two additional struts. The lengths of the leading-edge supporting lines, here named the kite bridle, are different; but the control bar, tether lengths, and experimental setup used for both kites are identical.

Both kites have a supported inflated leading edge and sweptback wing. The bridled leading edge allows for flatter wings with higher aspect ratios than those with unsupported ones, thus increasing the aerodynamic efficiency and projected lifting area. Moreover, the concave trailing edge and sweptback angle in the wing allow for greater lift control by increasing the pitch variations induced by the control bar. Such higher maneuverability still keeps acceptable control forces on the bar, due to the shifting of the attaching points of the control lines further back from the pressure center of the wing. These characteristics, in comparison with the so-called C-type unsupported leading-edge kites, provide a broader flight envelope and allow a larger dynamical range for the measured variables. Such a property is of great interest for future studies in terms of parameter identification and system observability. Figure 3a shows the 13 m^2 kite during one of the flight tests.

The flight-test instrumentation implemented in the experimental setup is split into two groups. The first group includes the onboard instruments. A PixHawk™ running Px4™ open-source flight control software is used for data logging the GPS position $\tilde{\boldsymbol{r}}$ and velocity $\tilde{\boldsymbol{v}}$, the magnetic field vector $\tilde{\boldsymbol{B}}$, static and differential pressures $\tilde{p}_0$ and $\tilde{p}_d$, specific forces $\tilde{\boldsymbol{f}}_{IMU}$, and angular rates $\tilde{\boldsymbol{\omega}}$. Additionally, Px4™ attitude estimation is recorded during the flight for validation purposes of our own estimator (see Fig. 4 in Sec. IV). Onboard instruments are powered by a 4.8 V nickel–metal hydride battery, whereas its positioning and orientation with respect to the kite frame S_B is guaranteed by a specifically designed three-dimensionally printed rig (see Fig. 3b). Such an interface allows us to safely attach the sensors to the central strut of the kite, just behind the leading edge. The plastic rig is designed to align the PixHawk hardware to the axes of S_K. Therefore, the measured vector components are provided in the S_K frame.

Table 1   Kite parameters

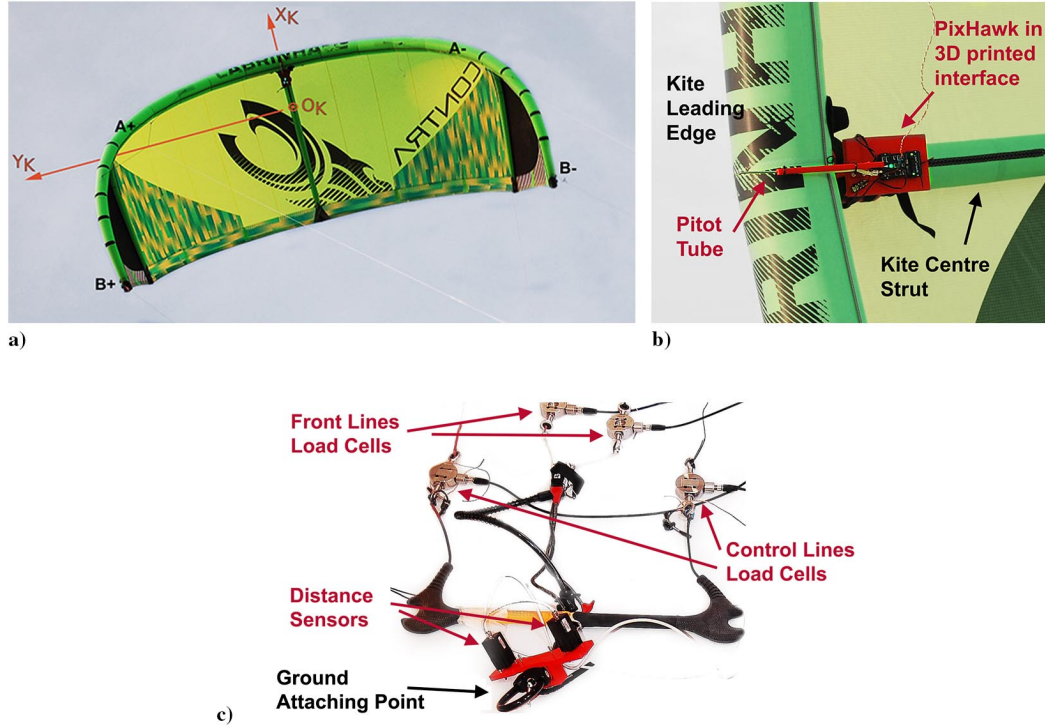|	Cabrinha Switchblade	Cabrinha Contra
Mass	3.4 kg	3.4 kg
I_x	8.68 kg/m^2	12.33 kg/m^2
I_y	2.43 kg/m^2	3.18 kg/m^2
I_z	8.40 kg/m^2	11.41 kg/m^2
I_{xz}	0.33 kg/m^2	0.43 kg/m^2
Surface	10 m^2	13 m^2
Span	4.3 m	5 m
Struts	5	3
X_A	0.42 m	0.53 m
Y_A	1.05 m	1.40 m
Z_A	−0.20 m	−0.31 m
X_B	−0.97 m	−0.98 m
Y_B	2.15 m	2.50 m
Z_B	1.38 m	1.60 m
L_l	23.85 m	24.37 m
L_t	23.19 m	23.45 m

a)

b)

c)

Ground
Attaching Point

Fig. 3   Kite (Fig. 3a), onboard instruments (Fig. 3b), and control bar (Fig. 3c) during a flight test.
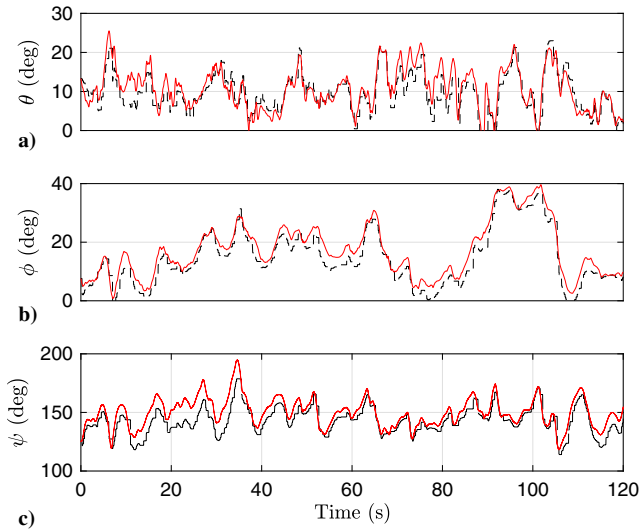

a)

b)

c)

Fig. 4   Euler angles from the PixHawk software (dashed lines) and the FPR algorithm (solid lines).

The second instrumentation group comprises the ground-based sensor equipment. As shown in Figs. 2 and 3c, four load sensors are installed to measure the tether tensions at points $S_{c\pm}$ and $S_{l\pm}$. The sensors at $S_{c\pm}$ are at distance s_0 from the tips of the control bar. To measure the state of the control vector, defined by the power ratio and the bar deflection, a specifically designed and manufactured interface with two Posiwire WS31C 750-mm-distance sensors is secured to the safety fuse of the kite control bar. These sensors measure the distances $d_\pm$ between the tips of the interface, placed at distance w_{cl} from a tether of length L_s, and the points $S_{c\pm}$.

Because $|\overline{C_0 O_K}| \gg |\overline{A_\pm B_\pm}|$, one may assume that the rear control lines practically belong to Π and they are parallel to the tether of length L_s. Under such assumptions, the following trigonometric relations hold:

$$d^2_\pm \pm \approx \left(L_{cl} + D_{cb} \mp \frac{L_c}{2} \sin \nu + s_0 \right)^2 + \left(\frac{L_c}{2} \cos \nu - w_{cl} \right)^2 \qquad (9)$$

These constraints and Eq. (8) give the power ratio u_p (or the control bar distance D_{cb}) and the bar deflection ν as a function of the measured distances d_+ and d_-.

Table 2 provides the numerical values of the characteristic lengths related to the experimental setup of the control bar. The load cells and the distance sensors feed a National Instruments (NI) 6002 data-acquisition system with eight 16-bit 50 kilosamples/s analog inputs and two 16-bit analog outputs. The data-acquisition system is connected to a laptop running NI Signal Express Software through a Universal Serial Bus (USB) interface.

The selection of the load cells was based on the expected traction forces. A conservative calculation, based on a maximum aerodynamic lift coefficient of $C_L = 1.2$ and an airspeed of about $V_a = 7$ m/s, gave a lift force of around 460 N for the larger kite. Because most of the load was supported by the front lines, we took two 50 kg self-amplified ± 10 V analog output, load cells for the front tethers. During flight tests, forces were consequently limited to 1000 N (roughly twice the expected stationary lift force) by manual control of the kite and real-time supervision of the generated forces.

Table 2   Characteristic lengths related with the control bar

Symbol	Value, m
L_c	0.56
L_{ds}	0.52
L_{cl}	0.1
s_0	0.35
L_s	2.07
L_{ps}	1.1
w_{cl}	0.07

For the rear tethers, two 10 kg-load cells were selected to measure control forces over the kite. The amplified load cells and the distance sensors were powered by a 22.2 V lithium polymer rechargeable battery pack, whereas the NI 6002 was powered through the host computer's USB port.

All the measured variables are logged during the flight and postprocessed offline. As two different groups of sensors (onboard and ground-based) with two different data-logging systems (PixHawk for onboard ground sensors and a NI data-acquisition system for on-ground sensors) are used, a synchronization method is needed. For this purpose, a square time signal is generated during the experiment by the analog output of the NI system. This signal, transported by an electrical wire attached to a front line, is sent from the NI system to the 6.6 V PixHawk Analog to digital converter input, and therefore synchronously records both on board and on the ground.

Finally, in the case of loss of control, surf kites are equipped with a manual safety fuse that allows the rear lines to become completely slack, so the kite flags on the front lines with a zero angle of attack and falls to the ground. To make this safety method compatible with the experimental setup, a fifth line linking the leading edge with the ground is added. This safety line, which has a low diameter, is long enough to be completely slack during the flight; and its influence on the kite dynamics is negligible (both inertial effects and aerodynamic drag).

III. Space State Flight-Path Reconstruction

This section presents a solution to the FPR problem of the experimental setup in Sec. II.B. Its main inputs are the digital records of the sensors during the flight, which contain statistical noise and other inaccuracies; and its outputs are the time histories of the system state variables. In addition to the kite kinematic variables, it provides an estimation of the kite aerodynamic force and moment, the wind speed and direction, and tether loads. This feature distinguishes it from other estimation solutions for kites, and it is of great interest for future works on the aerodynamic characterization of kites based on EBM techniques. The core of the algorithm follows previous works on FPR for aircraft by using continuous-discrete extended Kalman filters (EKFs), in which the forces and moments are also part of the state vector and modeled as Gauss–Markov stochastic processes [25,33,34]. They are adapted to consider the special characteristics of kites and our experimental setup. These extensions cover the information added by the constraints introduced by the tethers, the GPS, the magnetic field, and the tether length measurements, as well as a variation of the process model of the sensors, to include stochastic error models for each sensor.

The process model of the filter is written in the compact form:

$$\frac{d\boldsymbol{x}(t)}{dt} = \boldsymbol{f}_{\mathrm{proc}}[\boldsymbol{x}(t)] + \bar{G}w(t) \tag{10}$$

with $\boldsymbol{x}$ representing the state vector and $\boldsymbol{w}$ the process noise, which is modeled from a multivariable normal distribution function with zero mean and covariance $\bar{Q}$. Explicit equations for the flow $\boldsymbol{f}_{\mathrm{proc}}$ and the constant matrix $\bar{G}$ are given in the Appendix. The state vector of the filter

$$\boldsymbol{x} = \begin{bmatrix} \boldsymbol{x}_k & \boldsymbol{x}_{\mathrm{bias}} & \boldsymbol{\chi}_1 & \boldsymbol{\chi}_2 & \boldsymbol{\chi}_3 \end{bmatrix} \tag{11}$$

appearing in Eq. (10) includes 1) the kite state vector [$\boldsymbol{x}_k$ in Eq. (2)]; 2) a bias state vector $\boldsymbol{x}_{\mathrm{bias}} = \begin{bmatrix} \boldsymbol{\Theta}_B & \boldsymbol{\Theta}_f & \boldsymbol{\Theta}_\omega & \boldsymbol{\Theta}_{\mathrm{aer}} \end{bmatrix}$ with the biases for the measured magnetic field, inertial measurement unit (IMU)-specific forces, angular velocities, and airspeed; and 3) a set of three pseudostates vectors

$$\boldsymbol{\chi}_i = \begin{bmatrix} \boldsymbol{F}_{ai} & \boldsymbol{M}_{ai} & T_{A^+i} & T_{A^-i} & T_{B^+i} & T_{B^-i} & V_{wi} & \psi_{wi} \end{bmatrix}$$

with $i = 1, 2, 3$ stochastically described using third-order Markov models. The first vector $\boldsymbol{\chi}_1$ contains the S_B components of the aerodynamic force $\boldsymbol{F}_{a1}$ and moments about the center of mass of the kite $\boldsymbol{M}_{a1}$, the magnitudes of the tether tensions at the four attachment

points $T_{A^{\pm}1}$ and $T_{B^{\pm}1}$, the magnitude of the wind velocity $V_{w,1}$, and its heading angle $\psi_{w,1}$. The process equations of this vector and the ones for $\boldsymbol{\chi}_2$ and $\boldsymbol{\chi}_3$ yield a three-term quadratic interpolation as a function of time for which the coefficients are updated by the filter at each sampling instant. The dimensions of the kite state $\boldsymbol{x}_k$, bias state $\boldsymbol{x}_{\mathrm{bias}}$, and each Markov vector $\boldsymbol{\chi}_i$ are equal to 12, 10, and 12, respectively. Therefore, the dimension of the total state vector of the filter $\boldsymbol{x}$ is $N_F = 58$.

Although the state vector of the filter just contains the magnitude of the tether forces, we can estimate the vectors if we assume that the tensions are along the line determined by the attachment points ($A^{\pm}$ or $B^{\pm}$) and O_E. Hereafter, we will take

$$\boldsymbol{T}_{A^{\pm}} = -T_{A^{\pm}1}\overline{O_E A^{\pm}}/|\overline{O_E A^{\pm}}| \tag{12}$$

$$\boldsymbol{T}_{B^{\pm}} = -T_{B^{\pm}1}\overline{O_E B^{\pm}}/|\overline{O_E B^{\pm}}| \tag{13}$$

with

$$\overline{O_E A^{\pm}} = \boldsymbol{r} + \overline{O_K A^{\pm}} \tag{14}$$

$$\overline{O_E B^{\pm}} = \boldsymbol{r} + \overline{O_K B^{\pm}} \tag{15}$$

$$\overline{O_K A^{\pm}} = X_A \boldsymbol{i}_K \pm Y_A \boldsymbol{j}_K + Z_A \boldsymbol{k}_K \tag{16}$$

$$\overline{O_K B^{\pm}} = X_B \boldsymbol{i}_K \pm Y_B \boldsymbol{j}_K + Z_B \boldsymbol{k}_K \tag{17}$$

The coordinates of the attachment points of the two kites are given in Table 1. Equations (12) and (13) assume that the tethers are straight, and they use the fact that the tethers are much longer than the distance between the center of the mass of the kite and the IMU, as well as any distance related with the setup of the control bar (see Table 2). This pair of equations gives the tether tensions as a function of the state vector of the filter.

After denoting the observed variables with the symbols $\sim$, the observation model of the filter is

$$\tilde{\boldsymbol{y}} = \boldsymbol{h}(\boldsymbol{x}) + \boldsymbol{\eta} \tag{18}$$

with $\tilde{\boldsymbol{y}}$ representing the observation vector, $\boldsymbol{h}(\boldsymbol{x})$ representing the observation model that maps the true state space into the observed space (see the explicit model of $\boldsymbol{h}$ in the Appendix), and $\boldsymbol{\eta}$ representing the observation noise that is assumed to be zero mean Gaussian white noise with covariance $\bar{R}$. The observation vector of the experimental setup

$$\tilde{\boldsymbol{y}} = \begin{bmatrix} \tilde{\boldsymbol{r}} & \tilde{\boldsymbol{v}} & \tilde{\boldsymbol{f}}_{\mathrm{IMU}} & \tilde{\boldsymbol{\omega}} & \tilde{\boldsymbol{B}} & \tilde{v}_{\mathrm{aer}} & \tilde{D} & \tilde{T}_{A^-} & \tilde{T}_{B^+} & \tilde{T}_{B^+} & \tilde{T}_{A^+} \end{bmatrix} \tag{19}$$

includes the S_E components of the position and velocity vectors of the kite ($\tilde{\boldsymbol{r}}$ and $\tilde{\boldsymbol{v}}$); the S_K components of the specific force, the angular velocity, and the magnetic field ($\tilde{\boldsymbol{f}}_{\mathrm{IMU}}$, $\tilde{\boldsymbol{\omega}}$, and $\tilde{\boldsymbol{B}}$); the magnitude of the airspeed $\tilde{v}_{\mathrm{aer}}$; the distance between the fixed point O_E and the center of mass of the kite $\tilde{D}$; and the four magnitudes of the tether forces $\tilde{T}_{A^{\pm}}$ and $\tilde{T}_{B^{\pm}}$.

The application of the EKF to Eqs. (10–18) is standard (see, for instance, Ref. [35]). As usual, we will denote with superscripts − and + the a priori (before measurement) and a posteriori (after measurement) estimated values, respectively. Given the estimated value of the state vector $\hat{x}_j^+$ and the covariance matrix $\bar{P}_j^+$ at instant t_j, the EKF computes their values at a later instant t_{j+1} as follows. First, in the prediction phase, the reference trajectory $\boldsymbol{x}_R(t)$ is computed by integrating Eq. (10) without noise [the term $\boldsymbol{G}\boldsymbol{w}(t)$]

$$\frac{d\boldsymbol{x}_R(t)}{dt} = f_{\mathrm{proc}}[\boldsymbol{x}_R(t)] \tag{20}$$

from $t = t_j$ to $t = t_{j+1}$ and with the initial condition $x_R(t_j) = \hat{x}_j^+$. An approximation of the state transition matrix $\bar{\Phi}$ is obtained by integrating the linearized version of Eq. (20)

$$\frac{d\bar{\Phi}}{dt} = \bar{J}\,\bar{\Phi} \tag{21}$$

with initial condition $\bar{\Phi}(t = 0) = \bar{I}$, and $\bar{J}$ as the Jacobian of f evaluated at $\hat{x}_j^+$. The a priori state vector and covariance matrix at t_{j+1} are

$$x_{j+1}^- = x_R(t_{j+1}) \tag{22}$$

$$\bar{P}_{j+1}^- = \bar{\Phi}\bar{P}_j^+\bar{\Phi}^T + \bar{G}\,\bar{Q}\,\bar{G}^T \tag{23}$$

The Kalman gain is

$$\bar{K}_{j+1} = \bar{P}_{j+1}^- \bar{H}_{j+1}^T (\bar{H}_{j+1}\bar{P}_{j+1}^- \bar{H}_{j+1}^T + \bar{R})^{-1} \tag{24}$$

with $\bar{H}_{j+1}$ as the Jacobian of h evaluated at $\hat{x}_{j+1}^-$. The a posteriori (i.e., corrected by the measurements) estimations at t_{j+1} are

$$\hat{x}_{j+1}^+ = \hat{x}_{j+1}^- + \bar{K}_{j+1}[y_{j+1} - h(\hat{x}_{j+1}^-)] \tag{25}$$

$$\bar{P}_{j+1}^+ = (\bar{I} - \bar{K}_{j+1}\bar{H}_{j+1})\bar{P}_{j+1}^- \tag{26}$$

where y_{j+1} is the measurement vector provided by the sensor.

In addition to the Kalman innovation error $y_{j+1} - h(\hat{x}_{j+1}^-)$ in Eq. (25), the filter also gives the difference $h(\hat{x}_{j+1}^+) - h(\hat{x}_{j+1}^-)$ that can be used for checking purposes.

The application of the filter to our flight data exhibited a high robustness with little sensitivity to its initialization. In any case, we normally initialized x_k by using the information provided by the GPS and assuming symmetric flight with zero angular velocity. Vectors x_{bias}, χ_2, and χ_3 were initialized to zero. For χ_1, we set the specific forces equal to minus the weight, zero moments, and wind velocity and its heading angle taken from average measurements before the flight. Following [25], the covariance matrix was initialized with the measured noise of the measured variables, and it was initialed to one-fourth of the estimated initial value of the state for the unmeasured ones. The filter parameters had been tuned by using the sensor datasheets and by analyzing the effect of the different parameters on the filter output. A full description of the filter and the parameters used in this work are given in the Appendix and Table A1, respectively.

IV. Experimental Results

Flight tests have been carried out with the 13 and 10 m² kites under similar wind conditions. The testing procedure started by powering all the sensors while the kites were on the ground. Px4™ software was modified to record data from all sensors after powering up. Once a valid GPS signal was acquired, the kite was launched from one edge of the wind window and steered toward a stable equilibrium state close to the zenith. At that moment, the data-acquisition software and the synchronization time signal were started, thus allowing a synchronous data acquisition of the onboard and on-ground instruments. Several maneuvers (see the following) were performed repeatedly, and the kite was landed at one edge of the wind window afterward. The data recorded by all the instruments, which were resampled using a common 50 Hz time vector started at the first rising edge of the synchronization signal, were analyzed offline.

Figures 4a–4c show the evolution of the pitch, roll, and yaw angles for the 13 m² kite during the first 2 min of flight. The dashed lines and the solid lines correspond to the Px4™ and the FPR estimated attitudes, respectively. Both estimations, obtained from totally independent algorithms and software, are in good agreement with discrepancies in the estimated pitch and roll angles under 5 deg, and they are a little bit higher for yaw angles (especially at the beginning
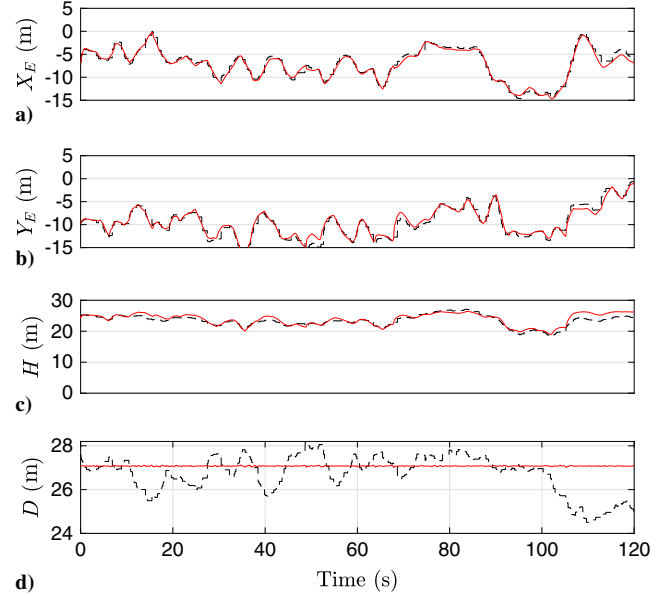

Fig. 5 Position and distance from the sensors (dashed lines) and the FPR algorithm (solid lines).

of the flight). They prove that the experimental setup and the filter are correctly implemented. A second verification of the integrity of the filter is given in Fig. 5, which shows the GPS measured (dashed lines) and FPR estimated (solid lines) values of the kite position components x_E and y_E, its altitude $H = -z_E$, and the constraint distance D appearing in Eq. (A9). The addition of such a constraint in our EKF greatly improves the GPS accuracy. As shown in Fig. 5d, the raw GPS distance to the attachment point O_E oscillates with typical GPS accuracy values, whereas the FPR solution follows the imposed constraint.

The next two sections show experimental results of the two different maneuvers: 1) a pullup, i.e., continuous enhancement of the power ratio with vanishing (or small) lateral deflection of the control bar; and 2) a steering maneuver with periodic variations of the deflection angle of the control bar. The goal of the analysis is twofold. First, it provides quantitative information about the performances of the experimental setup and the filter, and it shows coherence between the control inputs and kite response. Second, it highlights some of the distinguished features of the filter, such as the estimation of the aerodynamic force and moment.

A. Pullup Maneuver

Figure 6 shows the evolution of the power ratio and deflection angle of the control bar during a pullup maneuver of the 10 m² kite. As shown by the following results, the maneuver is not perfectly symmetric but close to it. The power ratio is increased smoothly from approximately 40 to 90%, and the deflection angle is held almost constant at -4 deg which shows a constant pulling on the right control line during the whole maneuver (the one linked to point B_- in Fig. 1). The position of the center of mass of the kite (not shown) remains almost constant during the time span displayed in Fig. 6.

The FPR of the Euler angles (pitch, yaw, and roll) versus the power ratio during the pullup maneuver is shown in Fig. 7a, in which, for clarity, the yaw angle is divided by a factor of 10. As expected, the yaw and roll angles are almost constant during the pullup, and the pitch angle increases notably ($\Delta\theta \sim 7.1$ deg). These results are in agreement with the sign of the estimated angular velocities (see Fig. 7b). The linear dependence between the pitch angle and the power ratio can be understood from simple kinematic considerations. After assuming straight and inextensible tethers, pure rotation along j_K, and small pitch angle variations, we can write $\Delta\theta \approx -\Delta D_{\text{cb}}/R_G$, with $\Delta\theta$ being the increment of the pitch angle, ΔD_{cb} the distance increment between the control bar and the power stopper, and
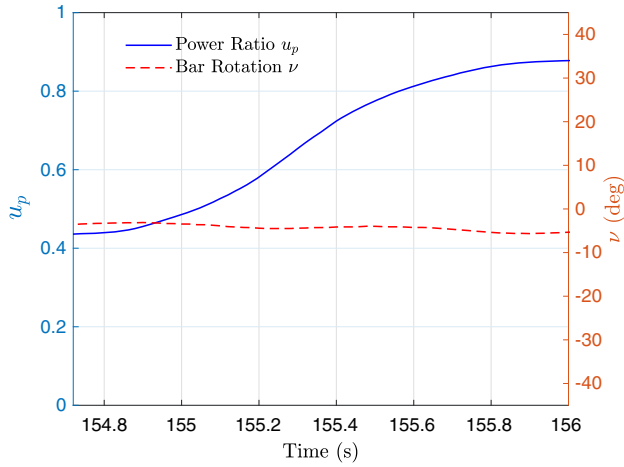
Fig. 6 Power ratio and bar deflection angle versus time during a symmetric pullup maneuver.
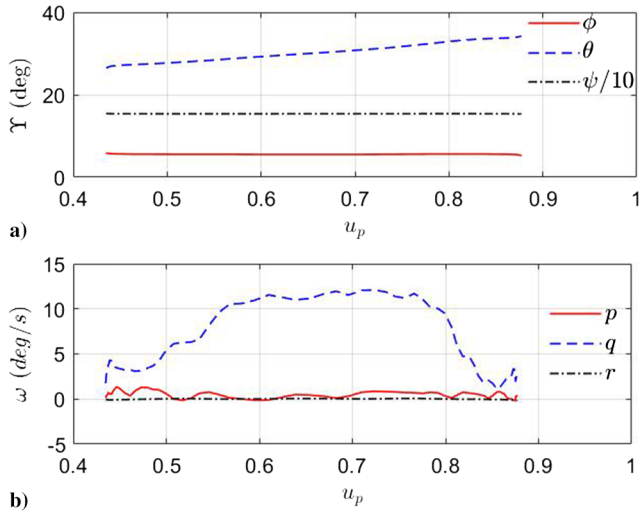

Fig. 7 Pullup maneuver: Euler angles and angular velocity versus power ratio.

$$R_G = \sqrt{(X_A - X_B)^2 + (Z_A - Z_B)^2} = 2.12 \text{ m}$$

the distance between the two lines passing through points A_+ and A_- and B_+ and B_- for the 10 m^2 kite. Calling $u_{p0} \approx 0.42$ and $u_{p\infty} = 0.9$ the initial and final power ratios, one has

$$\Delta D_{cb} = (L_s - L_{ps} - L_{ds})(u_{p0} - u_{p\infty}) \approx -0.216 \text{ m}$$

that gives a pitch increment of 5.84 deg.

A quasi-stationary ($\Delta t \approx 1.2$ s) variation of pitch angle translates into an instantaneous increase of the kite angle of attack and modifies the aerodynamic forces. Its lateral S_K components, F_{ay1} remains almost invariant, as shown by the dashed line in Fig. 8a. However, as expected, the longitudinal components F_{ax1} and F_{az1} increase considerably during the maneuver. Figure 8b shows the components of the estimated aerodynamic moment. The pitch moment M_{ay1} remains relatively constant, indicating a position of the center of mass close to the aerodynamic center $c/4$. This can be checked using the data provided in Table 1, in which $c/4 \approx (X_A - X_B)/4 = 0.38$ m, and the distance of the c.g. to the leading edge of the kite is approximately $X_A = 0.42$ m. On the other hand, an average wind heading angle of $\psi_w \approx -60$ deg and a yaw angle during the maneuver of $\psi \approx 150$ deg result in a negative sideslip angle of the
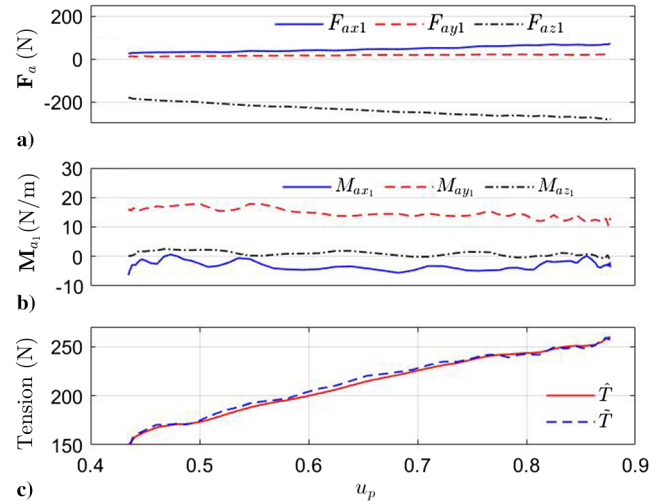

Fig. 8 Pullup maneuver: a,b) aerodynamic force and moment and c) total tension versus u_p.

kite. As expected, the estimated roll moment M_{ax1} is negative due to the negative dihedral of the wing. Finally, Fig. 8c shows the magnitude of the resultant of the four tether tensions estimated in the FPR $\hat{T}$ and, for reference, the tensions measured by the load sensors $\tilde{T}$. Again, the tension exhibits a linear dependence with the power ratio and is almost doubled during the pullup.

B. Steering Maneuver

The lateral-directional dynamics of the 10 m^2 kite was investigated by periodically varying the deflection angle of the control bar. As shown in Fig. 9, the maximum and minimum deflections were about 20 and -30 deg. Because the force at the bar increased notably during the induced crosswind motion of the kite, the pilot could not keep the power ratio constant and it varied periodically around the nominal value of $u_p \approx 0.4$. The kite flew in crosswind conditions and moved from side to side in the wind window. A top view of the measured trajectory is displayed in Fig. 10, in which we also plotted the wind direction and the Earth axes at the initial instant of the steering maneuver.

We now describe the lateral-directional steering maneuver as seen from the point of view of the pilot placed at the origin the wind reference frame displayed in Fig. 10. The steering maneuver started with the kite placed at the right side of the wind window (circle in Fig. 10). Because the kite initially had a lateral velocity pointing to
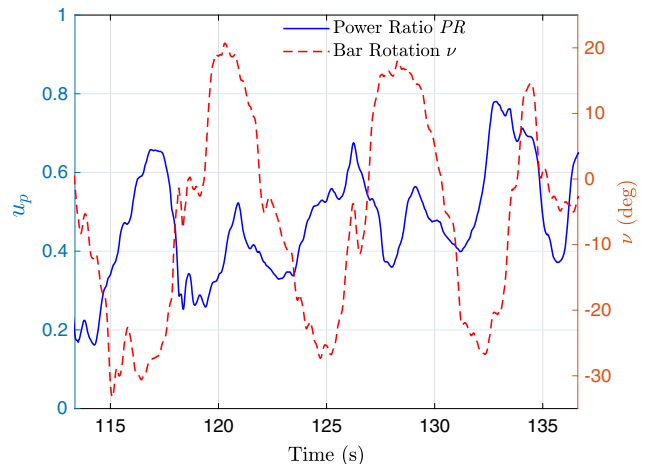

Fig. 9 Power ratio and bar deflection angle versus time during a steering maneuver.
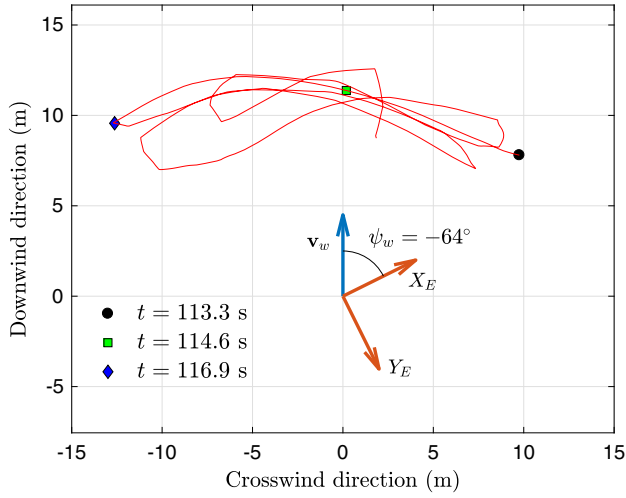
Fig. 10 Top view of the kite trajectory during the steering maneuver.

Fig. 12 Steering maneuver: a) evolution of the aerodynamic force, b) torque, and c) tether tension resultant.

the left and the pilot imposed almost zero deflection to the control bar at that instant, the kites moved laterally. Although the kite was moving to the left with a positive and increasing roll angle (Fig. 11a), the pilot pulled the right tip of the control bar, thus decreasing angle ν (see Fig. 9). Such a control input stopped the lateral motion of the kite, and it avoided a kite crash at the left-hand side of the wind window. The kite reached the center of the wind window and the maximum lateral displacement at instants of $t = 114.6$ s and $t = 116.9$ s, respectively. The latter coincided approximately with the minimum of ν. After reaching the maximum lateral displacement at the left side, the kite moved to the right and the pilot increased the value of ν from -27 deg at $t \approx 117$ s to $+20.46$ deg at 120.4 s. The kite performed a second crosswind motion during that time interval. It was also interesting to look at the behavior of the roll angular velocity component p. At the beginning of the maneuver, p was positive and at a maximum. The action of the pilot decreased the value of p and, once it vanished, the kite banked to the right and moved to the opposite side of the wind window.

An analysis of the control inputs in Fig. 9 and the Euler angles in Fig. 11 reveals a strong correlation between the deflection of the bar and the yaw angle of the kite. The roll response also follows these two variables but with certain delay. The forces and torques provided by the EKF (Figs. 12a and 12b) are coherent with the dynamics described previously. The lateral force component F_{ay1} and the roll torque M_{ax1} oscillate among positive and negative values. The
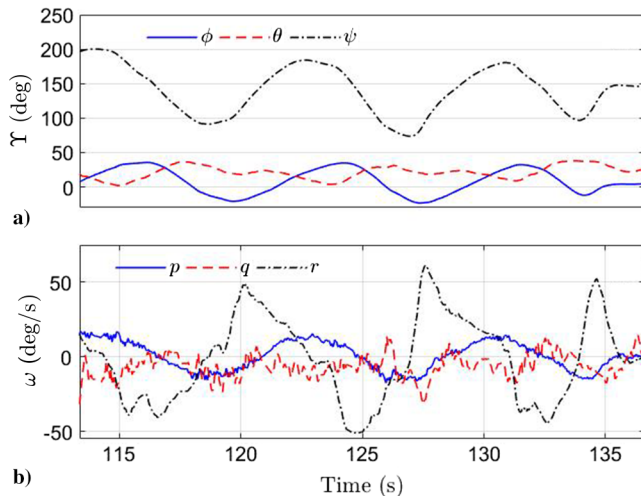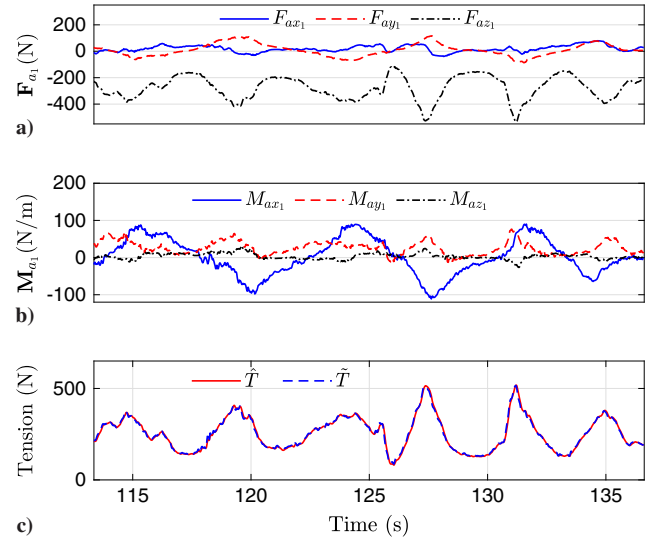
longitudinal force components, especially F_{az1}, are larger than the one observed during the pullup due to the crosswind conditions of the steering maneuver. This effect is also evident in Fig. 12c, in which the magnitude of the resultant of the four tether tensions is plotted.

Similar pullup and steering maneuvers have been recently analyzed theoretically with the module KiteSurf of the Lagrangian kite flight simulator named LAKSA. The dynamic response of the kite and the tether tensions found in the simulations were in qualitative agreement with the experimental results of this work [15]. A quantitative agreement will not be possible until an accurate aerodynamic model for the kites is available. The combination of our FPR algorithm with the estimation-before-modeling technique can contribute to this goal.

V.   Conclusions

This work presents a flight-path reconstruction method for tethered systems as well as an experimental setup designed to provide the required flight-test data for the algorithm. The solution of the flight-path reconstruction problem (also known as a compatibility check) is the optimal estimation of the system state-space trajectory, which is consistent with the kinematic equations of a kite, observed variables, and stochastic error models for the involved sensors. The method is very general and avoids several a priori hypotheses, such as the angular rate dependence on control inputs, the relative attitude of the kite to the tethers, and the compliance with a particular aerodynamic model. This feature distinguishes the proposed EKF from past works and, because the filter provides the aerodynamic force and torque, it represents the estimation step of the estimation before modeling technique in the aerodynamic parameter identification problem of a tethered aircraft. It can be also a fundamental component in closed-loop control scenarios.

Two important advantages of the experimental setup are the portability and low cost. Two kites of different sizes and stiffness are investigated with the experimental setup, which can be adapted to other kites or even to tethered drones by just three-dimensionally printing the corresponding interfaces to host the onboard measurement instruments. However, the analysis of the results suggests that a more precise platform for the aerodynamic characterization of kites can be achieved by implementing the following improvements: 1) adding an air data boom with sensors to measure the flow direction (wind vanes) and to improve the quality of the velocity magnitude by measuring in an undisturbed region of the flowfield, and 2) substituting the control bar and the load sensors at the tethers by a remotely controlled mechanical assembly with integrated load sensors. These changes would slightly affect the current EKF by extending the observation vector and the

Fig. 11   Steering maneuver: a) evolution of Euler angles and b) angular velocity.

models for the angle of attack and sideslip angle measured by the wind vanes.

Appendix: Estimator Description

A.1. Observation Model

This Appendix introduces the error and observation models that are needed to implement Eq. (18) in the EKF. The observed S_E components of the position and the velocity vectors are $\tilde{\boldsymbol{r}} = \tilde{x}_E \boldsymbol{i}_E + \tilde{y}_E \boldsymbol{j}_E + \tilde{z}_E \boldsymbol{k}_E$ and $\tilde{\boldsymbol{v}} = \tilde{v}_x \boldsymbol{i}_E + \tilde{v}_y \boldsymbol{j}_E + \tilde{v}_z \boldsymbol{k}_E$. After ignoring latency but including a wideband and not correlated noise, the GPS model reads

$$\begin{pmatrix} \tilde{x}_E \\ \tilde{y}_E \\ \tilde{z}_E \end{pmatrix} = \begin{pmatrix} x_E \\ y_E \\ z_E \end{pmatrix} + \boldsymbol{\eta}_r \tag{A1}$$

$$\begin{pmatrix} \tilde{v}_x \\ \tilde{v}_y \\ \tilde{v}_z \end{pmatrix} = \bar{R}_{\mathrm{EK}} \begin{pmatrix} u \\ v \\ w \end{pmatrix} + \boldsymbol{\eta}_v \tag{A2}$$

in which we introduce the rotation matrix that relates S_E and S_K vector components:

$$\bar{R}_{\mathrm{EK}} = \begin{pmatrix} c\psi c\theta & c\psi s\theta s\phi - s\psi c\phi & c\psi s\theta c\phi + s\psi s\phi \\ s\psi c\theta & s\psi s\theta s\phi + c\psi c\phi & s\psi s\theta c\phi - c\psi s\phi \\ -s\theta & c\theta s\phi & c\theta c\phi \end{pmatrix} \tag{A3}$$

and, for brevity, we write $s\alpha$ and $c\alpha$ to denote the sine and cosine of any angle α. We remark that the S_E components of the position vector in Eq. (A1) (x_E, y_E, and z_E) and the S_K components of the kite velocity in Eq. (A2) (u, v, and w) belong to the kite state vector $\boldsymbol{x}_k$. The noises in the right-hand side of Eqs. (A1) and (A2) are taken from normal distribution functions with zero means and variances $\sigma_{\eta_r}^2$ and $\sigma_{\eta_v}^2$, respectively.

After $\tilde{\boldsymbol{r}}$ and $\tilde{\boldsymbol{v}}$, the next two variables in the observation vector $\tilde{\boldsymbol{y}}$ are the specific forces and the angular velocity components in the kite frame. The model for these two vectors, is a postcalibration error model given by [36]

$$\tilde{\boldsymbol{f}}_{\mathrm{IMU}} = \frac{1}{m} \left[\boldsymbol{F}_{a1} + \sum_{i=\pm} (\boldsymbol{T}_{A^i} + \boldsymbol{T}_{B^i}) \right] + \boldsymbol{\Theta}_f + \boldsymbol{\eta}_f \tag{A4}$$

$$\tilde{\boldsymbol{\omega}} = \boldsymbol{\omega} + \boldsymbol{\Theta}_\omega + \boldsymbol{\eta}_\omega \tag{A5}$$

where $\boldsymbol{\eta}_f \in N(0, \sigma_{\eta_f}^2)$, $\boldsymbol{\eta}_\omega \in N(0, \sigma_{\eta_\omega}^2)$, and the tensions depend on the state vector of the filter according to Eqs. (12) and (13). Similarly, for the magnetometer and the modulus of the airspeed, we write

$$\tilde{\boldsymbol{B}} = \bar{R}_{\mathrm{EK}}^T \boldsymbol{B}_0 + \boldsymbol{\Theta}_B + \boldsymbol{\eta}_B, \qquad \boldsymbol{\eta}_B \in N(0, \sigma_{\eta_B}^2) \tag{A6}$$

$$\tilde{v}_{\mathrm{aer}} = \left| \bar{R}_{\mathrm{EK}} \boldsymbol{v} - v_{w,1} \begin{pmatrix} \cos\psi_{w,1} \\ \sin\psi_{w,1} \\ 0 \end{pmatrix} \right| + \Theta_{\mathrm{aer}} + \eta_{v_{\mathrm{aer}}},$$

$$\eta_{v_{\mathrm{aer}}} \in N(0, \sigma_{\eta_{v_{\mathrm{aer}}}}^2) \tag{A7}$$

where $\boldsymbol{B}_0$ is the magnetic field in the test area. We remark that the observed differential pressure $\tilde{p}_d$ is transformed into true air speed (TAS) by using

$$\mathrm{TAS} = \sqrt{\frac{2\tilde{p}_d}{\rho}} \tag{A8}$$

with $\rho = 1.15 \text{ kg/m}^2$ as the air density at the test area obtained from the International Standard Atmosphere [37]. The TAS is then used by the observation model as $\tilde{v}_{\mathrm{aer}}$.

The last component of the observation vector is the distance from O_E and the center of mass of the kite, and it arises from the constraint introduced by the tethers, for which the stiffness is very high. Such a constraint reads

$$\tilde{D} = |\boldsymbol{r}| + \eta_D, \qquad \eta_D \in N(0, \sigma_{\eta_D}^2) \tag{A9}$$

Unlike previous components of the observation vector, the distance $\tilde{D}$ is constant and equal to $L_s + \sqrt{L_l^2 - y_{A^+}^2}$, in which we neglect the small distance between the location of the IMU and O_K, and Y_A is the distance between the attachment point A^+ and the plane of symmetry of the kite.

Because the biases of the observed tether forces are considered to be comparatively small, our observation model for the tether reads

$$\tilde{T}_{A^\pm} = T_{A^\pm 1} + \eta_{T_{A^\pm}} \tag{A10}$$

$$\tilde{T}_{B^\pm} = T_{B^\pm 1} + \eta_{T_{B^\pm}} \tag{A11}$$

with $\eta_{T_{A^\pm}}$ and

$$\eta_{T_{B^\pm}} \in N(0, \sigma_{\eta_T}^2)$$

From Eqs. (A1–A7) and (A9), one finds the function $\boldsymbol{h}$ in Eq. (18). Vector $\boldsymbol{\eta}$ is

$$\boldsymbol{\eta} = [\boldsymbol{\eta}_r \quad \boldsymbol{\eta}_v \quad \boldsymbol{\eta}_f \quad \boldsymbol{\eta}_\omega \quad \boldsymbol{\eta}_B \quad \boldsymbol{\eta}_{v_a \mathrm{er}} \quad \boldsymbol{\eta}_D$$
$$\eta_{T_{A^+}} \quad \eta_{T_{A^-}} \quad \eta_{T_{B^+}} \quad \eta_{T_{B^-}}]^T \tag{A12}$$

and the covariance matrix $\bar{R}$ has zeros everywhere except at the diagonal:

$$\mathrm{diag}(\bar{R}) = \begin{bmatrix} \sigma_{\eta_r}^2 & \sigma_{\eta_r}^2 & \sigma_{\eta_r}^2 & \sigma_{\eta_v}^2 & \sigma_{\eta_v}^2 & \sigma_{\eta_v}^2 & \sigma_{\eta_f}^2 & \sigma_{\eta_f}^2 & \sigma_{\eta_f}^2 \\ \sigma_{\eta_v}^2 & \sigma_{\eta_\omega}^2 & \sigma_{\eta_\omega}^2 & \sigma_{\eta_B}^2 & \sigma_{\eta_B}^2 & \sigma_{\eta_B}^2 & \sigma_{\eta_{v_{\mathrm{aer}}}}^2 & \sigma_{\eta_D}^2 \\ \sigma_{\eta_T}^2 & \sigma_{\eta_T}^2 & \sigma_{\eta_T}^2 & \sigma_{\eta_T}^2 \end{bmatrix} \tag{A13}$$

A.2. Process Model

This Appendix describes in detail the form of the flux $\boldsymbol{f}_{\mathrm{proc}}$ and the noise appearing in the right-hand side of Eq. (10). The dynamics of the kite state vector $\boldsymbol{x}_k$ is governed by

$$\frac{\mathrm{d}}{\mathrm{d}t} \begin{pmatrix} x_E \\ y_E \\ z_E \end{pmatrix} = \bar{R}_{\mathrm{EK}} \begin{pmatrix} u \\ v \\ w \end{pmatrix}$$

$$\frac{\mathrm{d}}{\mathrm{d}t} \begin{pmatrix} u \\ v \\ w \end{pmatrix} = \begin{pmatrix} f_x \\ f_y \\ f_z \end{pmatrix} + \bar{R}_{\mathrm{EK}}^T \begin{pmatrix} 0 \\ 0 \\ g \end{pmatrix} + \begin{pmatrix} rv - qw \\ pw - ru \\ qu - pv \end{pmatrix} \tag{A14}$$

$$\frac{\mathrm{d}}{\mathrm{d}t} \begin{pmatrix} \phi \\ \theta \\ \psi \end{pmatrix} = \begin{bmatrix} p + (q\sin\phi + r\cos\phi)\tan\theta \\ q\cos\phi - r\sin\phi \\ (q\sin\phi + r\cos\phi)\sec\theta \end{bmatrix} \tag{A15}$$

$$\frac{d}{dt}\begin{pmatrix} p \\ q \\ r \end{pmatrix} = \bar{I}_{O_K}^{-1} \begin{bmatrix} M_x - I_{xz}qp + rq(I_y - I_z) \\ M_y + I_{xz}(p^2 - r^2) + pr(I_z - I_x) \\ M_z + I_{xz}qr + pq(I_x - I_y) \end{bmatrix} \quad (A16)$$

where g is the gravitational acceleration; $\bar{I}_{O_K}$ the tensor of inertia of the kite about its center of mass; and I_x, I_y, I_z, and I_{xz} are the nonzero components in S_K of $\bar{I}_{O_K}$. In the right-hand sides of Eqs. (A14) and (A16), we gather in the specific force

$$\boldsymbol{f} = f_x \boldsymbol{i}_K + f_y \boldsymbol{j}_K + f_z \boldsymbol{k}_K$$

and torque

$$\boldsymbol{M} = M_x \boldsymbol{i}_K + M_y \boldsymbol{j}_K + M_z \boldsymbol{k}_K$$

as the actions of the aerodynamic and tether forces. These two vectors depend on the state vector of the filter as follows:

$$\boldsymbol{f} = \frac{1}{m}\left[\boldsymbol{F}_{a1} + \sum_{i=\pm}(\boldsymbol{T}_{A^i} + \boldsymbol{T}_{B^i}) \right] \quad (A17)$$

$$\boldsymbol{M} = \boldsymbol{M}_{a1} + \sum_{i=\pm}(\overline{O_K A^{\pm}} \times \boldsymbol{T}_{A^i} + \overline{O_K B^{\pm}} \times \boldsymbol{T}_{B^i}) \quad (A18)$$

with $\boldsymbol{T}_{A^{\pm}}$ and $\boldsymbol{T}_{B^{\pm}}$ given by Eqs. (12) and (13), and $\overline{O_K A^{\pm}}$ and $\overline{O_K B^{\pm}}$ given by Eqs. (16) and (17).

The process models for the sensor biases are

$$\frac{d\boldsymbol{\Theta}_B}{dt} = 0 \quad (A19)$$

$$\frac{d\boldsymbol{\Theta}_f}{dt} = -\frac{\boldsymbol{\Theta}_f}{\tau_a} + \boldsymbol{w}_f \qquad \boldsymbol{w}_f \in N\left(0, \sigma_{w_f}^2\right) \quad (A20)$$

$$\frac{d\boldsymbol{\Theta}_{\omega}}{dt} = -\frac{\boldsymbol{\Theta}_{\omega}}{\tau_{\omega}} + \boldsymbol{w}_{\omega} \qquad \boldsymbol{w}_{\omega} \in N\left(0, \sigma_{w_{\omega}}^2\right) \quad (A21)$$

$$\frac{d\Theta_{aer}}{dt} = -\frac{\Theta_{aer}}{\tau_{aer}} + w_{aer} \qquad \boldsymbol{w}_{aer} \in N\left(0, \sigma_{w_{aer}}^2\right) \quad (A22)$$

Therefore, the correlated noise of the IMU ($\boldsymbol{\Theta}_f$ and $\boldsymbol{\Theta}_{\omega}$) is defined by first-order Gauss–Markov processes in which the variances of the driving noise $\sigma_{w_f}^2$ and $\sigma_{w_{\omega}}^2$ and the time constants τ_a and τ_{ω} are tuning parameters adjusted to overbound the Allan variance plot of correlated noise [36]. This methodology is convenient for low-cost sensors like the one used in our experiment. Following the methodology of Ref. [36], we find $\tau_a = \tau_{\omega} = 10$ s, $\sigma_{w_f} = 0.1$ m/s^2, and $\sigma_{w_{\omega}} = 0.01\pi/180$ rad/s.

The last process equations are the ones related with the three Markov state vectors $\boldsymbol{\chi}_i$. Because

$$\boldsymbol{\chi}_i = \begin{bmatrix} \boldsymbol{F}_{ai} & \boldsymbol{M}_{ai} & \boldsymbol{T}_{A^+i} & \boldsymbol{T}_{A^-i} & \boldsymbol{T}_{B^+i} & \boldsymbol{T}_{B^-i} & V_{wi} & \psi_{wi} \end{bmatrix}$$

each of these vectors has 12 components that we can denote as χ_{ij} with $i = 1, \ldots, 3$ and $j = 1, \ldots, 12$. The process equations can then be written in the compact form

$$\frac{d}{dt}\begin{pmatrix} \chi_{1j} \\ \chi_{2j} \\ \chi_{3j} \end{pmatrix} = \begin{pmatrix} 0 & 1 & 0 \\ 0 & 0 & 1 \\ 0 & 0 & 0 \end{pmatrix}\begin{pmatrix} \chi_{1j} \\ \chi_{2j} \\ \chi_{3j} \end{pmatrix} + \begin{pmatrix} \xi_{\chi_{1j}} \\ \xi_{\chi_{2j}} \\ \xi_{\chi_{3j}} \end{pmatrix} \quad (A23)$$

with $\xi_{\chi_{ij}}$ taken for $i = 1, 2, 3$ from normal distribution functions with zero mean and variances $\sigma_{\xi_{F_A}}^2, \sigma_{\xi_{M_A}}^2, \sigma_{\xi_T}^2, \sigma_{\xi_w}^2$, and $\sigma_{\xi_{\psi}}^2$ for $j = 1, 2, 3$, $j = 4, 5, 6$ $j = 7, 8, 9, 10$, $j = 11$, and $j = 12$, respectively.

Table A1   EKF parameters

Symbol	Value
σ_{w_f}	0.1 ms^{-2}
$\sigma_{w_{aer}}$	5.0 ms^{-1}
σ_{ξ_m}	15.0 N/m
$\sigma_{\xi_{\psi}}$	$\pi/180$ rad
σ_{η_v}	2.0 ms^{-1}
$\sigma_{\eta_{\omega}}$	$4.3\pi/180$ rad/s^{-1}
$\sigma_{\eta_{v_{aer}}}$	10 ms^{-1}
σ_{η_T}	10.0 N
$\sigma_{w_{\omega}}$	$0.01\pi/180$ rad/s^{-1}
$\sigma_{w_{\xi_a}}$	5.0 ms^{-2}
$\sigma_{v_{\xi_w}}$	0.5 ms^{-1}
σ_{η_r}	5.0 m
σ_{η_a}	0.2 ms^{-1}
σ_{η_B}	0.4 G
σ_{η_D}	0.001^{-3} m

From previous equations, one readily finds the flux $\boldsymbol{f}_{proc}$, the noise vector $\boldsymbol{w}$, and the matrix $\bar{G}$ in Eq. (10). For instance, one has

$$\boldsymbol{w} = \begin{bmatrix} \boldsymbol{w}_f & \boldsymbol{w}_{\omega} & w_{aer} & \xi_{\chi_{1,1}} & \cdots & \xi_{\chi_{1,12}}, \\ \xi_{\chi_{2,1}} & \cdots & \xi_{\chi_{2,12}}, & \xi_{\chi_{3,1}} & \cdots & \xi_{\chi_{3,12}} \end{bmatrix}^T \quad (A24)$$

$$\bar{G} = \begin{bmatrix} \bar{\boldsymbol{0}}_{15\times43} \\ \bar{I}_{43\times43} \end{bmatrix}_{58\times43} \quad (A25)$$

with $\bar{\boldsymbol{0}}$ as a matrix with zeros and $\bar{I}$ as the identity matrix. The covariance matrix $\bar{Q}$ has zeros everywhere except at the diagonal that reads

$$\text{diag}(\bar{Q}) = \begin{bmatrix} \sigma_{w_f}^2 & \sigma_{w_f}^2 & \sigma_{w_f}^2 & \sigma_{w_{\omega}}^2 & \sigma_{w_{\omega}}^2 & \sigma_{w_{\omega}}^2 & \sigma_{w_{aer}}^2 \\ \sigma_{\xi_{1,1}}^2 & \cdots & \sigma_{\xi_{1,12}}^2 & \sigma_{\xi_{2,1}}^2 & \cdots & \sigma_{\xi_{2,12}}^2 & \sigma_{\xi_{3,1}}^2 & \cdots & \sigma_{\xi_{3,12}}^2 \end{bmatrix}$$
$$(A26)$$

Table A1 summarizes the parameters used in the process and observation models of our EKF.

Acknowledgments

References

[1] Loyd, M. L., "Crosswind Kite Power," *Journal of Energy*, Vol. 4, No. 3, May 1980, pp. 106–111.
doi:10.2514/3.48021

[2] Cherubini, A., Papini, A., Vertechy, R., and Fontana, M., "Airborne Wind Energy Systems: A Review of the Technologies," *Renewable and Sustainable Energy Reviews*, Vol. 51, Nov. 2015, pp. 1461–1476.
doi:10.1016/j.rser.2015.07.053

[3] Schmehl, R., (ed.), *Airborne Wind Energy–Advances in Technology Development and Research*, Green Energy and Technology, 1st ed., Springer, Singapore, 2018.
doi:10.1007/978-981-10-1947-0

[4] Carpenter, H., "Tethered Aircraft System for Gathering Energy from Wind," U.S. Patent 6,254,034, July 2001.

[5] Williams, P., Lansdorp, B., and Ockesl, W., "Optimal Crosswind Towing and Power Generation with Tethered Kites," *Journal of

Guidance, Control, and Dynamics, Vol. 31, No. 1, Jan. 2008, pp. 81–93.
doi:10.2514/1.30089

[6] Payne, P., and McCutchen, C., "Self-Erecting Windmill," U.S. Patent 3,987,987, Oct. 1976.

[7] Felker, F., "Progress and Challenges in Airborne Wind Energy," *Book of Abstracts of the International Airborne Wind Energy Conference 2017*, edited by M. Diehl, R. Leuthold, and R. Schmehl, Univ. of Freiburg, Delft Univ. of Technology, Freiburg, Germany, Oct. 2017, p. 188.
doi:10.4233/uuid:4c361ef1-d2d2-4d14-9868-16541f60edc7

[8] Fagiano, L., and Marks, T., "Design of a Small-Scale Prototype for Research in Airborne Wind Energy," *IEEE/ASME Transactions on Mechatronics*, Vol. 20, No. 1, Feb. 2015, pp. 166–177.
doi:10.1109/TMECH.2014.2322761

[9] Sánchez, G., "Dynamics and Control of Single-Line Kites," *Aeronautical Journal*, Vol. 110, No. 1111, 2006, pp. 615–621.
doi:10.1017/S0001924000001470

[10] Groot, S. G. C. D., Breukels, J., Schmehl, R., and Ockels, W. J., "Modelling Kite Flight Dynamics Using a Multibody Reduction Approach," *Journal of Guidance, Control, and Dynamics*, Vol. 34, No. 6, Nov. 2011, pp. 1671–1682.
doi:10.2514/1.52686

[11] Gros, S., and Diehl, M., "Modeling of Airborne Wind Energy Systems in Natural Coordinates," *Airborne Wind Energy*, edited by U. Ahrens, M. Diehl, and R. Schmehl, Springer, Berlin, 2013, pp. 181–203.
doi:10.1007/978-3-642-39965-7

[12] Gohl, F., and Luchsinger, R. H., "Simulation Based Wing Design for Kite Power," *Airborne Wind Energy*, edited by U. Ahrens, M. Diehl, and R. Schmehl, Springer, Berlin, 2013, pp. 325–338.
doi:10.1007/978-3-642-39965-7_10

[13] Alonso-Pardo, J., and Sánchez-Arriaga, G., "Kite Model with Bridle Control for Wind-Power Generation," *Journal of Aircraft*, Vol. 52, No. 3, April 2015, pp. 917–923.
doi:10.2514/1.C033283

[14] Pastor-Rodríguez, A., Sánchez-Arriaga, G., and Sanjurjo-Rivo, M., "Modeling and Stability Analysis of Tethered Kites at High Altitudes," *Journal of Guidance, Control, and Dynamics*, Vol. 40, No. 8, May 2017, pp. 1892–1901.
doi:10.2514/1.G002550

[15] Sánchez-Arriaga, G., Pastor-Rodríguez, A., Borobia-Moreno, R., and Schmehl, R., "A Constraint-Free Flight Simulator Package for Airborne Wind Energy Systems," *Journal of Physics: Conference Series*, Vol. 1037, No. 6, 2018, Paper 062018, http://stacks.iop.org/1742-6596/1037/i=6/a=062018.

[16] Salord Losantos, L., and Sánchez-Arriaga, G., "Flight Dynamics and Stability of Kites in Steady and Unsteady Wind Conditions," *Journal of Aircraft*, Vol. 52, No. 2, 2015, pp. 660–666.
doi:10.2514/1.C032825

[17] Sánchez-Arriaga, G., García-Villalba, M., and Schmehl, R., "Modeling and Dynamics of a Two-Line Kite," *Applied Mathematical Modelling*, Vol. 47, July 2017, pp. 473–486.
doi:10.1016/j.apm.2017.03.030

[18] Bosch, A., Schmehl, R., Tiso, P., and Rixen, D., "Dynamic Nonlinear Aeroelastic Model of a Kite for Power Generation," *Journal of Guidance, Control, and Dynamics*, Vol. 37, No. 5, June 2014, pp. 1426–1436.
doi:10.2514/1.G000545

[19] Folkersma, M., Schmehl, R., and Viré, A., "Fluid-Structure Interaction Simulations on Kites," *Book of Abstracts of the International Airborne Wind Energy Conference 2017*, edited by M. Diehl, R. Leuthold, and R. Schmehl, Freiburg, Germany, 2017, p. 144.
doi:10.4233/uuid:4c361ef1-d2d2-4d14-9868-16541f60edc7

[20] de Wachter, A., "Deformation and Aerodynamic Performance of a Ram-Air Wing," M.Sc. Thesis, Delft Univ. of Technology, Delft, The Netherlands, 2008.

[21] Milne, G., Soijer, M., Juliana, S., Hermansyah, M., and Mulder, J., "Maximum Likelihood Stability and Control Derivative Identification of a Cessna Citation II," AIAA Paper 2001-4013, 2001.
doi:10.2514/6.2001-4013

[22] Lichota, P., and Lasek, M., "Maximum Likelihood Estimation for Identification of Aircraft Aerodynamic Derivatives," *Archive of Mechanical Engineering*, Vol. 60, No. 2, 2013, pp. 219–230.
doi:10.2478/meceng-2013-0014

[23] Schmidt, E., Lellis, M. D., Saraiva, R., and Trofino, A., "State Estimation of a Tethered Airfoil for Monitoring, Control and Optimization," *IFAC-PapersOnLine, 20th IFAC World Congress*, Vol. 50, No. 1, 2017, pp. 13,246–13,251.
doi:10.1016/j.ifacol.2017.08.1960

[24] Ramachandran, S., Schneider, H., Mason, J., and Stalford, H., "Identification of Aircraft Aerodynamic Characteristics at High Angles of Attack and Sideslip Using the Estimation Before Modeling/EBM/ Technique," *Guidance, Navigation, and Control and Co-Located Conferences*, AIAA Paper 1977-1169, Aug. 1977.
doi:10.2514/6.1977-1169

[25] Hoff, J. C., and Cook, M. V., "Aircraft Parameter Identification Using an Estimation-Before-Modelling Technique," *Aeronautical Journal*, Vol. 100, No. 997, 1996, pp. 259–268.
doi:10.1017/S000192400002889X

[26] Mulder, J., Chu, Q., Sridhar, J., Breeman, J., and Laban, M., "Non-Linear Aircraft Flight Path Reconstruction Review and New Advances," *Progress in Aerospace Sciences*, Vol. 35, No. 7, 1999, pp. 673–726.
doi:10.1016/S0376-0421(99)00005-6

[27] Licitra, G., Burger, A., Williams, P., Ruiterkamp, R., and Diehl, M., "Optimum Experimental Design of a Rigid Wing AWE Pumping System," *56th IEEE Conference on Decision and Control*, IEEE Publ., Piscataway, NJ, Dec. 2017, pp. 4018–4025.
doi:10.1109/CDC.2017.8264250

[28] Licitra, G., Bürger, A., Williams, P., Ruiterkamp, R., and Diehl, M., "System Identification of a Rigid Wing Airborne Wind Energy System," arXiv:1711.10010, Nov. 2017.

[29] Hummel, J., "Automatisierte Vermessung und Charakterisierung der Dynamischen Eigenschaften Seilgebundener, Vollflexibler Tragflachen," Ph.D. Dissertation, Technische Univ. Berlin, Berlin, 2017.

[30] Oehler, J., and Schmehl, R., "Experimental Characterization of a Force-Controlled Flexible Wing Traction Kite," *Book of Abstracts of the International Airborne Wind Energy Conference 2017*, edited by M. Diehl, R. Leuthold, and R. Schmehl, Albert Ludwig Univ. Freiburg and Delft Univ. of Technology, Freiburg, Germany, 2017, p. 125.
doi:10.4233/uuid:4c361ef1-d2d2-4d14-9868-16541f60edc7

[31] Fagiano, L., Huynh, K., Bamieh, B., and Khammash, M., "On Sensor Fusion for Airborne Wind Energy Systems," *IEEE Transactions on Control Systems Technology*, Vol. 22, No. 3, May 2014, pp. 930–943.
doi:10.1109/TCST.2013.2269865

[32] Fagiano, L., Zgraggen, A. U., Morari, M., and Khammash, M., "Automatic Crosswind Flight of Tethered Wings for Airborne Wind Energy: Modeling, Control Design, and Experimental Results," *IEEE Transactions on Control Systems Technology*, Vol. 22, No. 4, July 2014, pp. 1433–1447.
doi:10.1109/TCST.2013.2279592

[33] Sri-Jayantha, M., and Stengel, R. F., "Determination of Nonlinear Aerodynamic Coefficients Using the Estimation-Before-Modeling Method," *Journal of Aircraft*, Vol. 25, No. 9, Sept. 1988, pp. 796–804.
doi:10.2514/3.45662

[34] Goszczyński, J. A., Michalski, W. J., and Pietrucha, J. A., "Estimation Before Modelling as the Method for Identification of the Aircraft Aerodynamic Characteristics in Nonlinear Flight Regime," *Journal of Theoretical and Applied Mechanics*, Vol. 38, No. 1, 2000, pp. 107–120.

[35] Welch, G., and Bishop, G., "An Introduction to the Kalman Filter," Dept. of Computer Science, Univ. of North Carolina at Chapel Hill, Chapel Hill, NC, 1995.

[36] Xing, Z., and Gebre-Egziabher, D., "Modeling and Bounding Low Cost Inertial Sensor Errors," *2008 IEEE/ION Position, Location and Navigation Symposium*, Monterey, CA, May 2008, pp. 1122–1132.
doi:10.1109/PLANS.2008.4569999

[37] ICAO, "Manual of the ICAO Standard Atmosphere: Extended to 80 Kilometres (262,500 Feet)," 3rd ed., International Civil Aviation Organization (ICAO), Doc 7488/3, 1993.